한국측량학회지 제27권 제1호 2009. 2 : 723~733

Extraction of Geometric Components of Buildings with Gradients-driven Properties

Suyoung Seo[1] · Byung-Guk Kim[2]

Abstract

This study proposes a sequence of procedures to extract building boundaries and planar patches through segmentation of rasterized lidar data. Although previous approaches to building extraction have been shown satisfactory, there still exist needs to increase the degree of automation. The methodologies proposed in this study are as follows: Firstly, lidar data are rasterized into grid form in order to exploit its rapid access to neighboring elevations and image operations. Secondly, propagation of errors in raw data is taken into account for in assessing the quality of gradients-driven properties and further in choosing suitable parameters. Thirdly, extraction of planar patches is conducted through a sequence of processes: histogram analysis, least squares fitting, and region merging. Experimental results show that the geometric components of building models could be extracted by the proposed approach in a streamlined way.

Keywords : lidar data, rasterization, building model, segmentation, building boundary, planar patch

1. Introduction

For the last decades, usage of lidar data has been growing rapidly in a wide range of applications because of their capability of mapping surface models in a fast and accurate way (Huising and Gomes Pereira, 1998; Schenk, 1999; Schenk et al., 2001; Seo, 2003; Seo and O' Hara, 2008). Further, lidar data have been shown advantageous in generating three-dimensional models of buildings because of their direct delivery of elevation information without a matching process.

Lee (2006) conducted point clustering by region growing in a Triangulated Irregular Network (TIN). Filin and Pfeifer (2006) utilized a Hough transform to collect normal vectors from a single individual patch with proximity and local slopes. Forlani et al. (2006) extracted planar patches using image-based region growing and RANdom Sample Consensus (RANSAC) algorithm. Rottensteiner (2003) segmented roof planes based on normal vectors and expanded them by region growing. Jung et al. (2008) performed building boundary extraction using anisotropic diffusion filter and extracted planar patch extraction based on moving average, standard deviation, and slope angle among neighboring pixels. Lee et al. (2008) extracted patches using 3D Hough transform and refined them by reselecting patch pixels according to distance deviations.

With this background, this paper proposes a sequence of procedures to delineate building boundaries and to extract planar patches while considering following aspects. Firstly, error bounds inherent in raw lidar data are taken into account for. Secondly, consistency in setting parameter values over data area is observed. Thirdly, processes are performed on rasterized data structure to save the time for searching neighboring elevations. Fourthly, extraction of planar patches is performed by sequential histogram analyses of plane parameters. Fig. 1 illustrates the processing flow of the proposed approach in this study.

2. Rasterization of Lidar Data

2.1. Interpolation of Raw Lidar Data

Various options are possible for interpolating elevations at grid pixels using surrounding data points, such as an IDW (inverse distance weighting), a nearest-neighbor, and a linear interpolation based on a TIN structure. Fig. 2 illustrates point data and sur-

1) Research Fellow, Korean Land Spatialization Group, Inha University, Incheon 402-751, Korea(E-mail:syseo@inha.ac.kr)
2) Director, Korean Land Spatialization Group, Inha University, Incheon 402-751, Korea(E-mail:byungkim@inha.ac.kr)

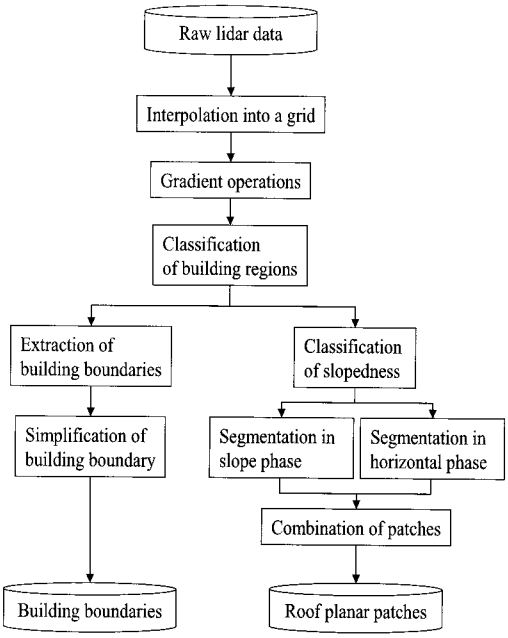

Fig. 1. Processing flow of the proposed approach in this study.

faces derived from those interpolations. Regarding the quality of surfaces, the linear interpolation method can be said superior to the others in planar regions such as building roofs. Thus, this study proposes the linear interpolation so that resulting surface is suitable to extract planar surface patches (Fig. 2(d)).

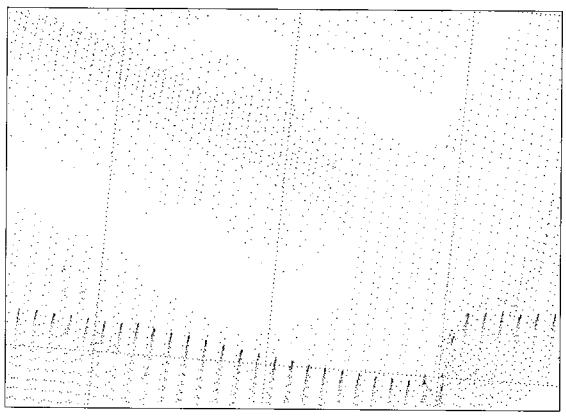

(a)

2.2 Generation of Gradient Images

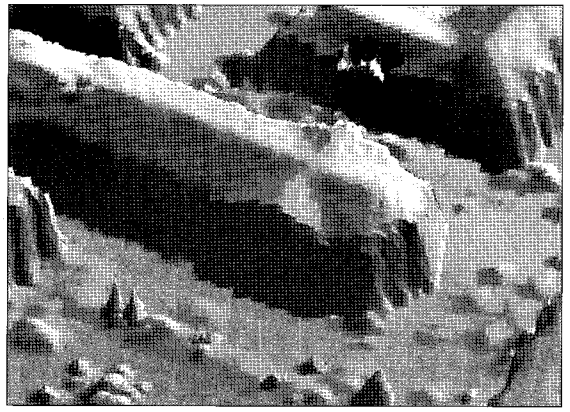

(b)

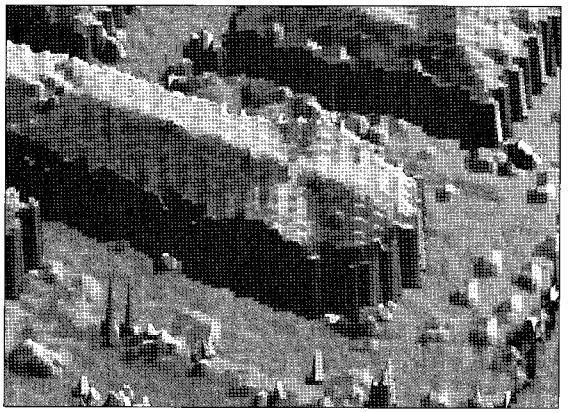

(c)

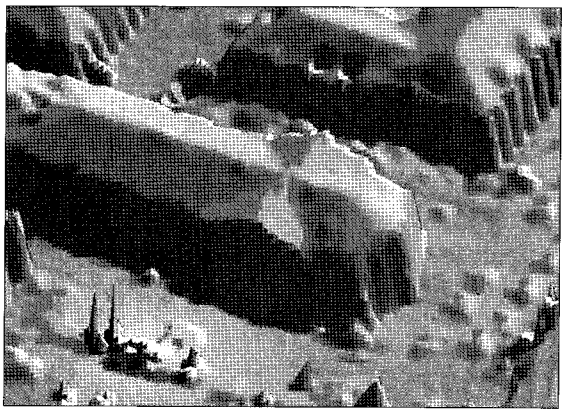

(d)

Fig. 2. Three-dimensional views of surfaces generated from different interpolation methods: (a) raw points and (b), (c), and (d) interpolated surfaces generated by IDW, nearest neighbor, and linear interpolations, respectively.

In order to exploit slopes in processing lidar data, gradient images are prepared as follows. Sobel edge operations are applied to the interpolated elevation image. Here, given pixel size c, to make gradient values correspond to the slopes in the real world, resulting values are normalized by dividing them by $2 \cdot c$ as:

$$g_X = [(Z_{i+1,j+1} + 2Z_{i,j+1} + Z_{i-1,j+1}) - (Z_{i+1,j-1} + 2Z_{i,j-1} + Z_{i-1,j-1})]/(4 \cdot 2 \cdot c)$$
$$g_Y = [(Z_{i+1,j-1} + 2Z_{i+1,j} + Z_{i+1,j+1}) - (Z_{i-1,j-1} + 2Z_{i-1,j} + Z_{i-1,j+1})]/(4 \cdot 2 \cdot c) \quad (2)$$

If the accuracy of elevation measurements is assumed to be σ_Z^2, the accuracy of gradient values derived is expected to be $\frac{3}{4}\sigma_Z^2$ by error propagation.

Azimuth and elevation angle at each pixel are derived from the gradients as shown in Fig. 3. Azimuth angle λ and elevation angle φ are computed as:

$$\lambda = \tan^{-1}\left(\frac{-g_Y}{-g_X}\right)$$
$$\varphi = \cos^{-1}\left(\frac{1}{\sqrt{g_X^2 + g_Y^2 + 1}}\right) \quad (3)$$

whereby λ is an angle measured in a full circle range of $[-\pi, \pi]$.

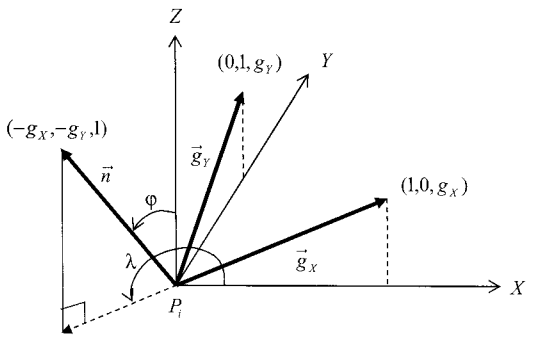

Fig. 3. Azimuth and elevation angles of the surface composed of the gradient vectors.

The accuracy of azimuth and elevation angles can be derived by error propagation as:

$$D\{\lambda\} = \begin{bmatrix} \frac{\partial\lambda}{\partial g_X} & \frac{\partial\lambda}{\partial g_Y} \end{bmatrix} \begin{bmatrix} \sigma_{g_X}^2 & 0 \\ 0 & \sigma_{g_Y}^2 \end{bmatrix} \begin{bmatrix} \frac{\partial\lambda}{\partial g_X} \\ \frac{\partial\lambda}{\partial g_Y} \end{bmatrix} = \frac{3}{2(g_X^2 + g_Y^2)}\sigma_Z^2$$
$$D\{\varphi\} = \begin{bmatrix} \frac{\partial\varphi}{\partial g_X} & \frac{\partial\varphi}{\partial g_Y} \end{bmatrix} \begin{bmatrix} \sigma_{g_X}^2 & 0 \\ 0 & \sigma_{g_Y}^2 \end{bmatrix} \begin{bmatrix} \frac{\partial\varphi}{\partial g_X} \\ \frac{\partial\varphi}{\partial g_Y} \end{bmatrix} = \frac{3}{(g_X^2 + g_Y^2 + 1)^2}\sigma_Z^2 \quad (4)$$

From the derivations above, errors in the two angles are shown to be functions of gradients and the measurement accuracy of raw data σ_Z^2. Azimuth measurements, however, can be interpreted to become unreliable more seriously as gradient magnitude gets closer to 0. This effect will be considered in segmenting planar patches from gradient images later in this paper. Fig. 4 shows an example of images derived by the Sobel gradient operations along the X and Y axes and the azimuth and elevation angles of each plane containing the gradient vectors at a pixel. In Fig. 4(c), azimuths in sloped surfaces are shown to be distinct while those in horizontal surfaces noisy.

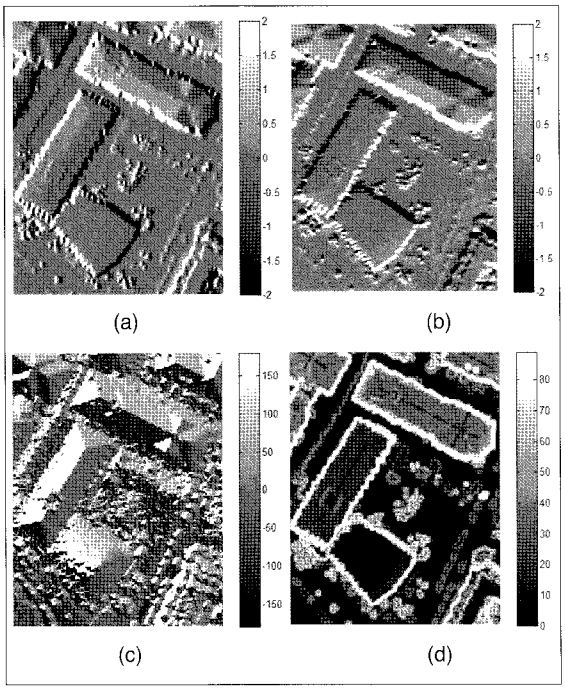

Fig. 4. Images derived from gradient operations: (a) gradient along the X axis, (b) gradient along the Y axis, (c) azimuth, and (d) elevation angle of the plane containing the two gradient vectors.

3. Extraction of Building Boundaries

3.1 Detection of Building Regions

With the images prepared in the foregoing processes, classification of data area into ground and non-ground regions can be performed. Firstly, non-steep regions are extracted with steep regions as their boundaries. Secondly, adjacent relationships among non-steep regions are derived. Thirdly, their elevation differences are analyzed so that their region type can be determined into low and high regions.

For the first process, a certain value for thresholding elevation angles is determined. Regarding the threshold, a low threshold value will make the regions more fragmented while a high threshold value may cause failures in distinguishing different objects. To find an optimal value, a few experiments were implemented and a value which corresponds to slope of 1.5 m/m was shown to be optimal from experiments. Table 1 summarizes the values of parameters predefined for the procedure. The rationale for this value is that most buildings are higher than 1.5 m against their surrounding terrain along their boundary and slopes of planar patches in building roofs are usually found to be lower than this value.

Table 1. Parameter values specified for extraction of building boundaries.

Parameter	Value
Minimum Slope	1.5 m/m
Minimum Building Size	50 m^2
Maximum Building Size	2500 m^2
Maximum Deviation in a Boundary	1.0 m

Secondly, pixels whose elevation angles are lower than the threshold are grouped using 8-connectivity and regions of which size are less than 50 m^2 or larger than 2500 m^2 are disregarded. Valid regions are labeled and dilated so that all the pixels classified as steep are filled completely with them.

Thirdly, classification is performed by computing the sum of all the elevation differences along the boundary of a candidate region. For a region i with its neighboring regions j=1,..,N, relative average elevation difference, μ_i of region i, is computed as:

$$\mu_i(\Delta z)=\frac{\sum_{j=1}^{N}[\mu_{ij}(\Delta z)\cdot n_{ij}]}{\sum_{j=1}^{N} n_{ij}} \quad (5)$$

where $\mu_i(\Delta z)$ and n_{ij} are the average elevation difference and the number of boundary pixels between regions i and j, respectively. The process classifies region i into a high region if its relative elevation difference, $\mu_i(\Delta z)$ is positive.

Fig. 5 shows in 2-D and 3-D that building and terrain regions could be successfully classified into high and low regions. Regions classified into high regions are taken as building regions and segmented further in the following processes.

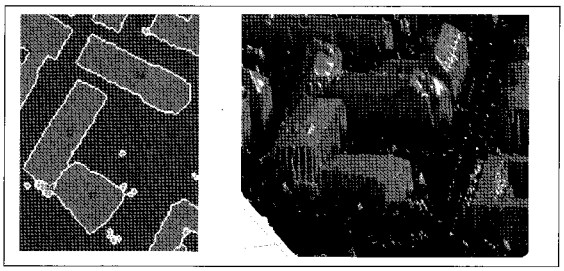

Fig. 5. Regions classified by relative elevation difference.

3.2 Simplification of Building Boundaries

Once building regions are identified, their boundaries are extracted and simplified. Firstly, building boundary pixels are traced and their row and column coordinates are recorded into a list in a sequential order. Then, each building boundary is segmented into straight lines.

The simplification strategy is to mark a point whose deviation is largest from a given straight line in a recursive way (Haralick and Shapiro, 1992). Fig. 6 demonstrates an example resulting from the boundary segmentation procedure.

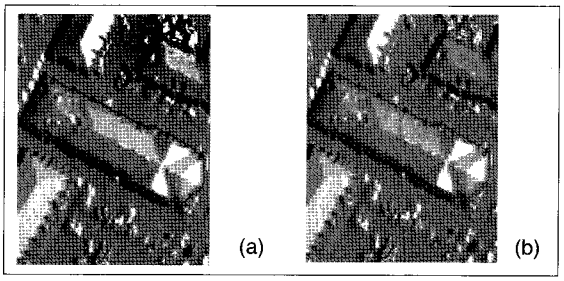

Fig. 6. Simplified building boundaries.

4. Segmentation of Building Roofs

4.1 Classification of Roof Pixels

For segmenting a building roof, azimuth values can be used as a strong cue for grouping pixels originated from a single surface patch. As stated in Section 2.2, however, azimuth value at a pixel whose gradient magnitude is small is not reliable. Thus, this study proposes segmentation of a roof surface in two phases: horizontal and sloped phases.

Firstly, every pixel whose gradient magnitude is lower than a predefined slope is classified as horizontal. A suitable tolerance for the gradient magnitude can be derived from Eq. (4). With consideration of accuracy reports about lidar observations, random errors of raw points are assumed to be 0.15m. Thereafter, the maximum tolerance of gradient magnitude for a pixel to belong to a horizontal surface was derived to be about 0.18 m/m. Table 2 summarizes the values of parameters predefined for segmentation.

Fig. 7 shows an example of horizontal pixels in Fig. 7(b) for a building region. From visual inspection, the building roof appears to be horizontal in the DSM, but closer inspection of the profile shown in Fig. 7(c) reveals that it can be divided into several planar patches.

Table 2. Parameter values specified for segmentation of building roofs.

Parameter	Value
Minimum Slope for Slope Phase	0.18 m/m
Maximum Azimuth Change	21.2°
Minimum Patch Size	5 pixels
Azimuth Bin Size	10.0°
Azimuth Tolerance	15.0°
Elevation Angle Bin Size	5.0°
Elevation Angle Tolerance	10.0°
Perpendicular Distance Bin Size	0.1 m
Perpendicular Distance Tolerance	0.2 m
Least Squares Fitting Tolerance	0.2 m
Maximum RMSE for Merging	0.2 m

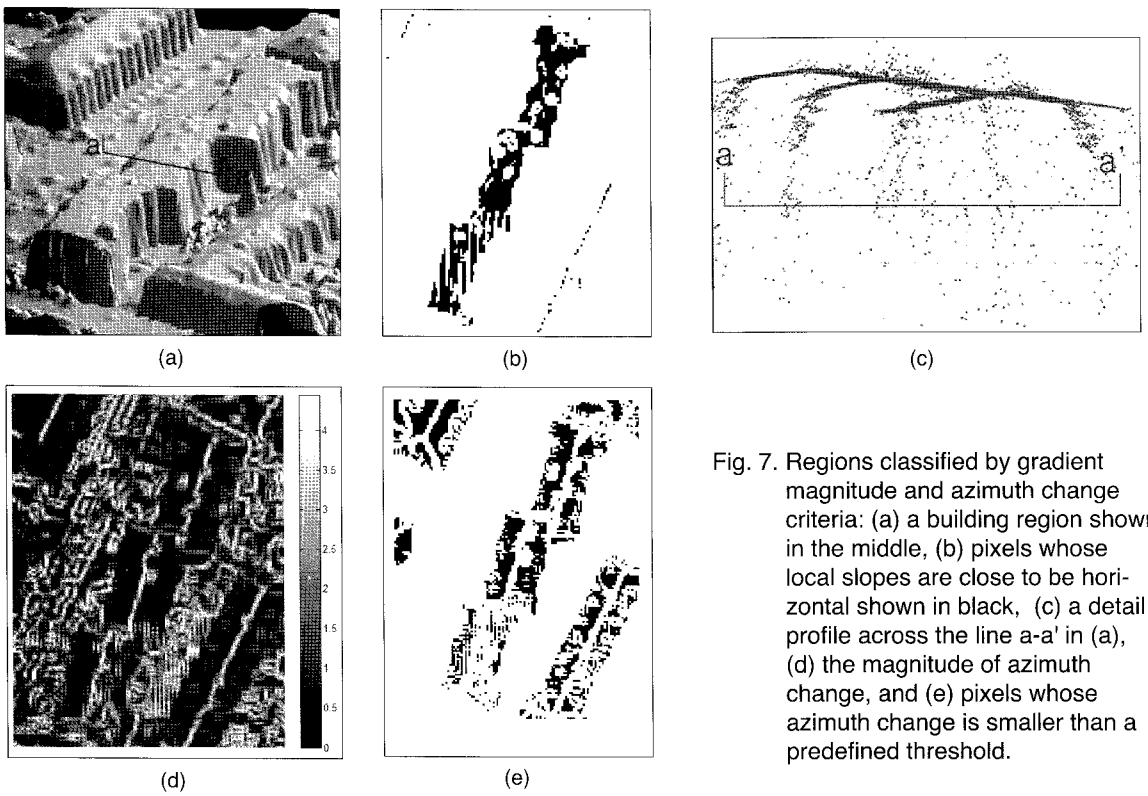

(a) (b) (c)

(d) (e)

Fig. 7. Regions classified by gradient magnitude and azimuth change criteria: (a) a building region shown in the middle, (b) pixels whose local slopes are close to be horizontal shown in black, (c) a detail profile across the line a-a' in (a), (d) the magnitude of azimuth change, and (e) pixels whose azimuth change is smaller than a predefined threshold.

To overcome the problem, seed regions are also extracted by azimuth changes. In detail, the magnitude of azimuth change at pixel (i,j), $|\Delta\lambda_{i,j}|$ is derived as follows. Let azimuths at pixels $(i+1, j-1)$ and $(i-1, j+1)$ be $\lambda_{i+1,j-1}$ and $\lambda_{i-1,j+1}$, respectively, and their difference be $\Delta\lambda_1$. Likewise, let $\Delta\lambda_2$ be the difference of the azimuths of pixels $(i+1, j+1)$ and $(i-1, j-1)$. Then, the magnitude of azimuth change $|\Delta\lambda_{i,j}|$ can be computed as:

$$|\Delta\lambda_{i,j}| = \left(\frac{\Delta\lambda_1^{\,2} + \Delta\lambda_2^{\,2}}{2} \right)^{1/2} \quad (6)$$

Fig. 7(d) shows an example of azimuth changes computed for the area shown in Fig. 7(a). As can be seen in Fig. 7(d), edges between two adjacent patches in the roof region become well distinguished, especially in its upper part. In this study, an angle of $30°/\sqrt{2} \approx 21.2°$ is chosen as a suitable threshold for the magnitude of azimuth change since it is large enough to avoid over-segmentation but less than angles between planar patches that can be observed in most building roofs. Fig. 7(e) shows an example of sloped pixels. Here, it is illustrated that although the pixels are close to be horizontal, they could be separated well.

In horizontal phase, candidate pixels are obtained directly by the thresholding of the slope magnitude image. In sloped phase, however, those are acquired through a sequential reselection procedure described in the following section.

4.2 Extraction of Planar Pixels in Slope Phase

In slope phase, planar patches are searched for progressively by applying following multiple conditions in a sequence: azimuth, elevation angle, perpendicular distance and planar surface fitting residuals.

Firstly, the patch extraction process reselects pixels based on azimuth (λ) in a sloped region. A histogram of azimuths is generated with a predefined bin size and its mode is determined. Then, pixels whose azimuth is close to the azimuth mode are selected and grouped into connected regions. Fig. 8 shows the histogram of azimuths in a long roof region with bin size (λ_b), $10°$. Fig. 9 depicts its sloped sub-regions bounded by the azimuth change.

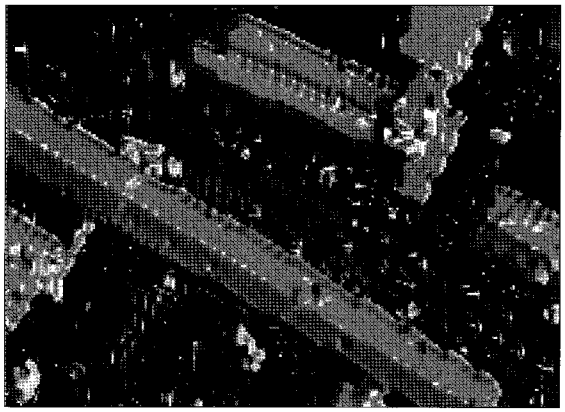

(a)

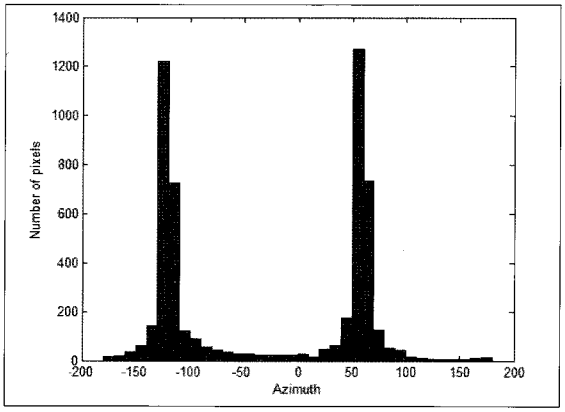

(b)

Fig. 8. Example of azimuth distributions in a roof region.

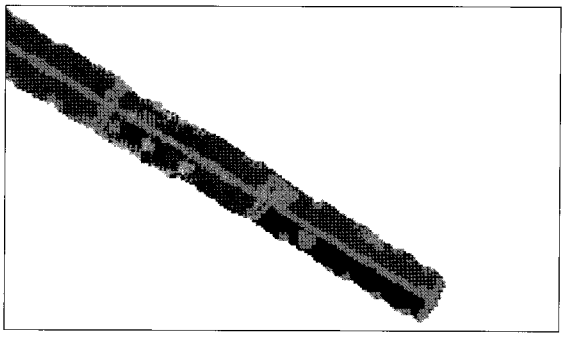

(a)

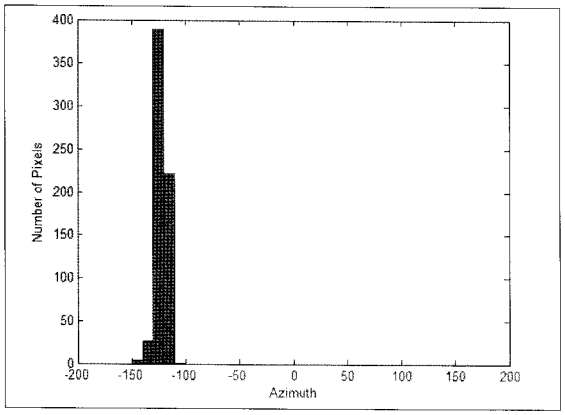

(b)

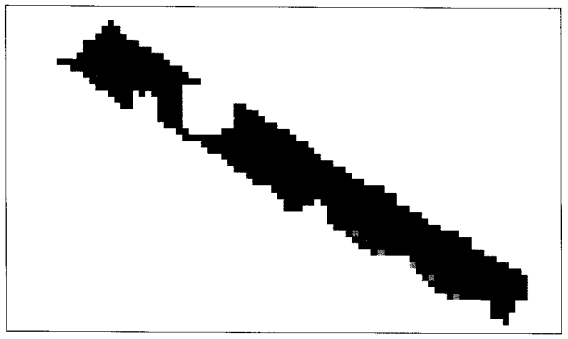

(c)

Fig. 9. Example of pixel reselection by the azimuth condition.

Secondly, the pixels selected in the above process are examined by elevation angle (φ) condition. Fig. 10 shows a histogram of elevation angles.

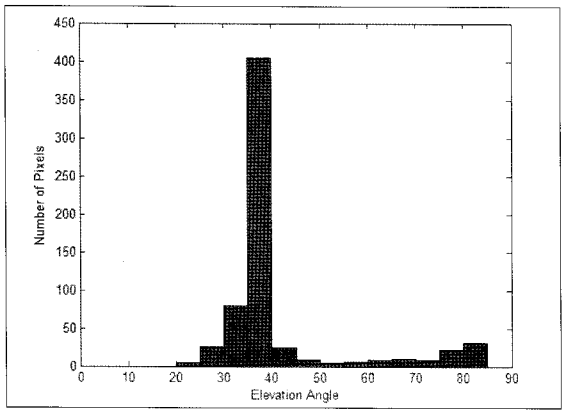

(a)

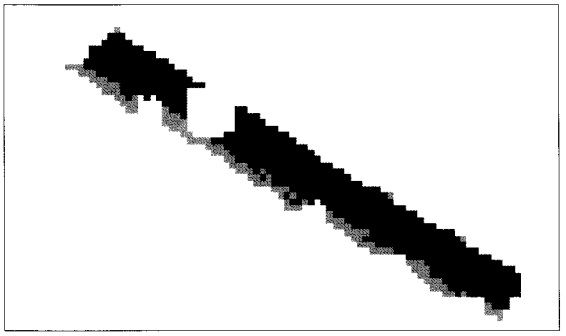

(b)

Fig. 10. Example of pixel reselection by the elevation angle condition: (a) histogram of the elevation angles of pixels shown in black in Fig. 9(c), (b) pixels reselected by elevation angle condition shown in black.

Thirdly, three-dimensional perpendicular distance (d) to a surface patch is employed to refining pixel selection. Let the unit normal vector to the plane be $\vec{n}$. Then, the normal vector and a perpendicular distance from point $(X_i - X_0, Y_i - Y_0, Z_i - Z_0)$ to the three-dimensional plane can be computed as:

$$\vec{n} = \left(\sin\varphi_\mu \cos\lambda_\mu, \sin\varphi_\mu \sin\lambda_\mu, \cos\varphi_\mu\right)$$
$$d_i = \vec{n} \cdot \left(X_i - X_0, Y_i - Y, Z_i - Z_0\right) \tag{7}$$

Fig. 11 shows an example of pixel reselection by perpendicular distance condition.

Once the pixels sharing a single plane are determined, a labeling process makes the pixels grouped into separated regions. Then, larger regions are processed with priority in the subsequent processes.

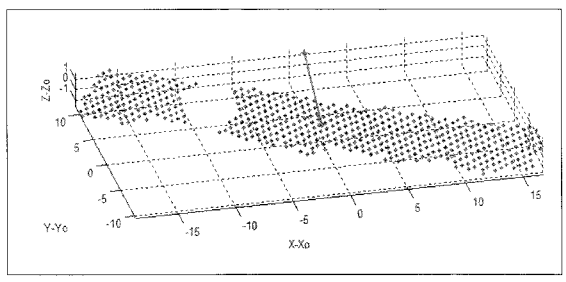

(a)

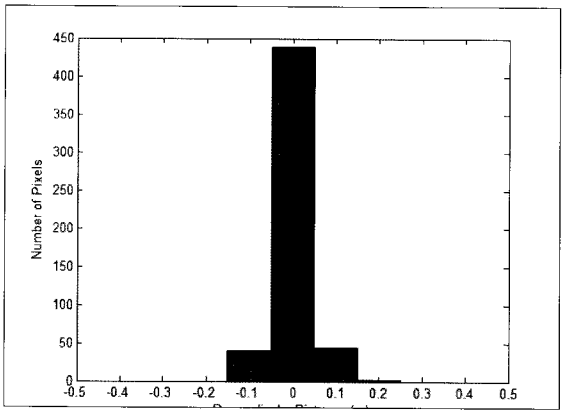

(b)

Fig. 11. Example of pixel reselection by the perpendicular distance condition.

4.3 Reselection of Planar Pixels by Least Squares Fitting

Once candidate pixels which are likely to compose a three-dimensional planar patch are obtained in the above processes, pixel selections are further refined and extended by least squares adjustment, whereby all parameters of a single three-dimensional plane are considered simultaneously. With least squares fitting, selection of planar patch pixels is performed as follows. The pixel regions originated from the foregoing processes are called *triggering regions* in this paper.

Firstly, planar parameters are estimated with a set of points (X_i, Y_i, Z_i) , i =1,...,N derived from candidate pixels. Let S_X, S_Y and Z_o be the plane parameters to be estimated in the following observation equations, expressed as:

$$\begin{bmatrix} Z_1 \\ Z_2 \\ \vdots \\ Z_N \end{bmatrix} = \begin{bmatrix} X_1 & Y_1 & 1 \\ X_2 & Y_2 & 1 \\ \vdots & \vdots & \vdots \\ X_N & Y_N & 1 \end{bmatrix} \begin{bmatrix} S_X \\ S_Y \\ Z_o \end{bmatrix} + \begin{bmatrix} e_{Z_1} \\ e_{Z_2} \\ \vdots \\ e_{Z_N} \end{bmatrix} \tag{8}$$

With matrix notations, formula for parameter estimation can be expressed as:

$$\begin{aligned} & y = A\xi + e, \qquad e \sim (0, \sigma_Z{}^2 I_N) \\ & N = A^T A, c = A^T y \\ & \hat{\xi} = N^{-1} c \\ & \tilde{e} = y - A\hat{\xi} \end{aligned} \tag{9}$$

Before proceeding to the next step, the condition number of the normal matrix N is checked to avoid singularity caused by distribution of points in a line.

Secondly, residuals $\tilde{e}$ for all the candidate points are computed and only the points whose residuals are within a predefined tolerance are selected. In this study, the residual tolerance was set to 0.2 m. Then, their corresponding pixels are connected in regions and pixels in the largest one are inspected further. The geometric distribution of the pixels to be inspected is again checked by the condition number stated above.

Thirdly, planar parameters are recomputed using only the points reselected and the slope of the plane is checked if it is lower than a predefined maximum slope, 1.5 m/m in order to discard steep patches which are more likely to be originated from building walls.

Fourthly, the plane determined in the previous step is used to collect all the pixels in the current building region whose displacement from it is within a tolerance. In resulting regions composed of the selected pixels, only the regions having overlaps with triggering pixels are considered and then the largest one is selected as the final patch.

Fifthly, the final patch extracted is saved and the pixels in the patch are categorized into processed pixels and subtracted from the list of pixels in the triggering region pixels and from that in the current building region pixels in the next iteration. Then, the extraction is performed with the rest of pixels in the current triggering region until there are no more pixels which may compose any valid patch. Once extraction of patches in the current triggering region is completed, the process performs extraction in the next triggering region, however with only the remaining pixels in the current building region being checked further.

Fig. 12 shows examples of the points resulting from pixel reselection by the least squares fitting process. As can be seen, starting with triggering regions, pixel selection could find the pixels in the roof regions whose height is consistent to the triggering region surface.

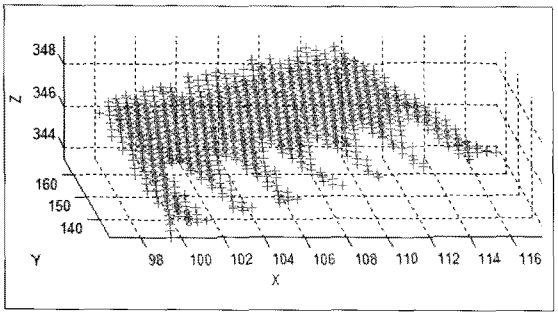

Fig. 12. Example of finding pixels in a plane by the least squares fitting process.

4.4 Combination of Extracted Patches

After planar patches are extracted based on sloped and horizontal triggering regions, they need to be combined to complete patch extraction over each roof region. Fig. 13 shows however, some examples of conflicts between patches obtained in two phases. To resolve this problem, this study first lays patches from sloped phase and fill the rest of a roof region with horizontal patches. Although this process makes some horizontal patches separated over patches from sloped phase, most of them can be recombined through the subsequent merging process described in the following.

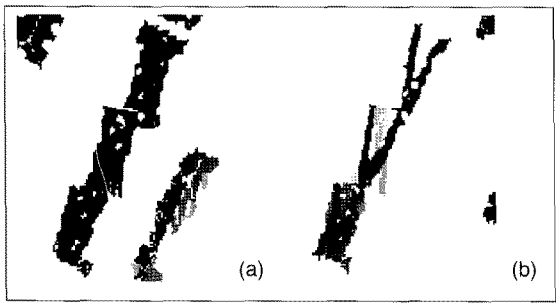

Fig. 13. Comparison of patches extracted from sloped and horizontal triggering regions.

Firstly, adjacency of regions are established with 4-connectivity. Secondly, the largest patch is selected among the current patches as a gathering patch and its planar parameters are estimated. Thirdly, the process selects a patch adjacent to the gathering patch. Then, residuals of its pixels against the gathering plane are computed and the patch is determined to be merged if their RMSE is within a tolerance which was set to 0.2 m in this study. Fourthly, all patches determined to be merged are combined into the gathering patch and the process selects the next gathering patch and find patches to be merged among the rest of patches which are not yet determined to be merged.

Fig. 14 illustrates an example of the combining process. As can be seen, patches in Fig. 14(c) which were separated after composition of sloped and horizontal ones in Figs. 14(a) and 14(b) are shown to be merged in Fig. 14(d).

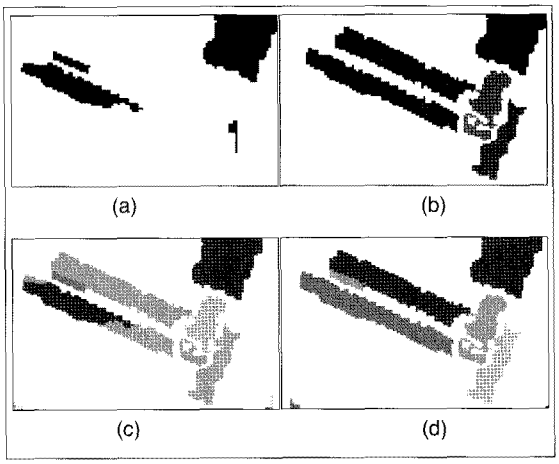

Fig. 14. Merging adjacent patches: (a) patches extracted from sloped phase, (b) patches from horizontal phase, (c) regions composed of patches from both phases, and (d) regions after merging adjacent patches.

5. Implementation and Discussion

5.1 Test Data

For testing the approach proposed, test data were obtained from a website managed by ISPRS Commission III Working Group 3 (http://www.itc.nl/isprswgIII-3/filtertest/index.html). Fig. 15(a) visualizes distribution of the raw points in the test data and Table 1 summarizes the properties of the data.

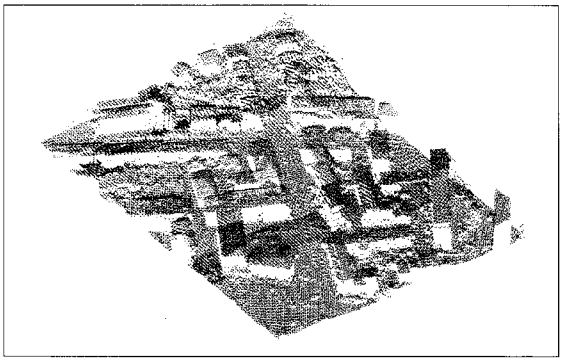

(a)

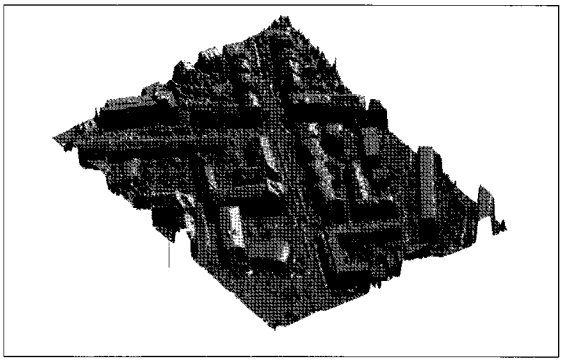

(b)

Fig. 15. Visualization of raw points in the test data and its DSM derived by interpolation.

Table 2. Properties of the test data.

Property	Description
Sensor	Optech laser scanner
No. Points	52,119
X and Y Spans	204 m by 264 m
Point Density	0.97 points/m^2

5.2 Experimental Results

Sobel gradient operations were implemented along the X and Y axes and their results were used to derive azimuth and elevation angles shown in Fig. 16. Then, through comparison of the elevations of neighboring pixels along region boundaries, a total of 39 regions were classified into building regions and their outlines simplified as shown in Fig. 17.

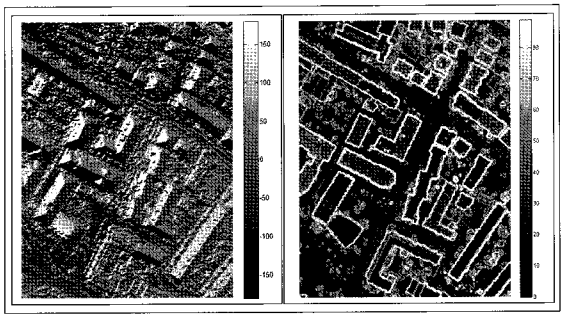

Fig. 16. Azimuth and elevation angle images over the study area.

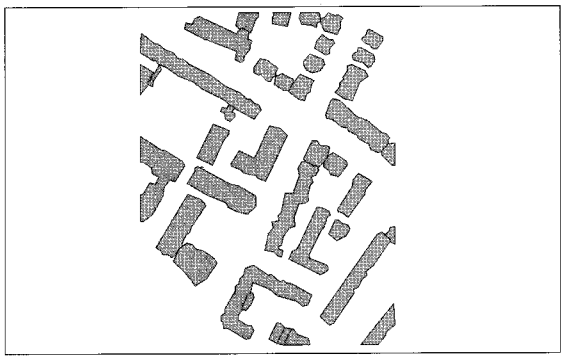

Fig. 17. Building boundaries extracted from the test area.

Within all the building regions, planar patches were extracted in both sloped and horizontal modes and combined, resulting in a total of 188 planar patches shown in Fig. 18. For assessing the quality of the resulting patches against their size, the variance component stated in Eq. (12) was estimated for every patch that has at least 4 raw points. In Fig. 19(a), the estimates of are shown to range from about 3 to 11 cm. As the patch size increases, however, the estimates appear to get closer to about 5 cm. These statistics may suggest that the accuracy of raw data might be better than the nominal lidar data accuracy of 15 cm. The figure states that the interpolation process to convert raw points into regular grid points tend to reduce the variance of lidar data at grid posts in individual patches with a certain degree of increase of redundancy in case the grid size is smaller than the average spacing of raw data.

6. Conclusion and Future Work

In this paper, a sequence of procedures for extraction of building boundaries and planar patches based on analysis of geometric

properties of rasterized lidar data were presented. To overcome the ambiguity of planar patch extraction caused by gradient variations in local area, planar patches were extracted in horizontal and sloped modes and merged with a strategy. From the experiment, it has been proven that the proposed procedures are applicable to general building models. Implementation of the procedures shows that processing is computationally efficient. Also, the parameters were determined reliably by taking account for domain knowledge and error propagation.

With those geometric components derived from this study, it is needed to assemble them to generate complete building models while considering the error bounds of those components and domain knowledge about building structure to obtain accurate building models in an efficient way.

Acknowledgement

This research was supported by a grant (08KLSGB01) from Cutting-edge Urban Development - Korean Land Spatialization Research Project funded by Ministry of Land, Transport and Maritime Affairs of Korean government.

References

Haralick, R. M. and Shapiro, L. G (1992), Computer and Robot Vision, Vol. I, Addison-Wesley, 672 p.

Huising, E. J. and Gomes Pereira, L. M. (1998), Errors and accuracy estimates of laser data acquired by various laser scanning systems for topographic applications, ISPRS J. Photogrammetry & Remote Sensing, Vol. 53, pp. 245-261.

Filin, S. and Pfeifer, N. (2006), Segmentation of airborne laser scanning data using a slope adaptive neighborhood, ISPRS J. Photogrammetry & Remote Sensing, Vol. 60, pp. 71-80.

Forlani, G., Nardinocchi, C., Scaioni, M. and Zingaretti, P. (2006), Complete classification of raw LIDAR data and 3D reconstruction of buildings, Pattern Analysis & Applications, Vol. 8, pp. 357-374.

Jung, H. S., Lim, S. B. And Lee, D. C. (2008), Utilizing airborne LiDAR data for building extraction and superstructure analysis for modeling, Korean Journal of Geomatics, Vol. 26, No. 3, pp. 227-239.

Lee, I. (2006), Segmentation of airborne LIDAR data: from points to patches, Korean Journal of Geomatics, Vol. 24, No. 1, pp. 111-121.

Lee, Y. J., Oh, J. H., Shin, S. W. and Cho, W. S. (2008), The segmentation and the extraction of precise plane equation of building roof plane using 3D Hough transform of LiDAR data, Korean Journal of Geomatics, Vol. 26, No. 1, pp. 505-512.

Rottensteiner, F. (2003), Automatic generation of high-quality building models from lidar data, IEEE Computer Graphics and Applications, Vol. 23, pp 42-50.

Schenk, T. (1999), Photogrammetry and laser altimetry, Int. Arch. Photogramm. Remote Sens., Vol. 32(3/W14), pp. 3-12.

Schenk, T., Seo, S. and Csatho, B. (2001), Accuracy study of airborne laser scanning data with photogrammetry, Int. Arch. Photogramm. Remote Sens., Vol. 34 (3/W4), pp. 113-118.

Seo, S. (2003), Model-based automatic building extraction from lidar and aerial imagery, Ph.D. Dissertation, The Ohio State University, Ohio.

Seo, S. and O' Hara, C. G. (2008), Parametric investigation of the performance of lidar filters using different surface contexts, Photogrammetric Engineering & Remote Sensing, Vol. 74, pp. 343-362.

(접수일 2009. 01. 29, 심사일 2009. 02. 13, 심사완료일 2009. 02. 24)